Journal of Mines, Metals and Fuels, *73(10): 3247-3266; 2025. DOI: 10.18311/jmmf/2025/50036*

Online ISSN : 0022-2755

Journal of Mines, Metals and Fuels

Contents available at: *www.informaticsjournals.co.in/index.php/jmmf*

Influence of Fly Ash and Coarse Aggregate Proportions on Fracture Parameters of Alkali Activated Self-Compacting Concrete

T. M. Channappa*, M. H. Prashanth, Mattur C. Narasimhan, R. G. Yatish, and Gundupalli Bhanu Prakash

National Institute of Technology Karnataka, Surathkal, Mangalore - 575025, Karnataka, India; channappatm@gmail.com

Abstract

Alkali-Activated Self-Compacting Concrete (AASCC) offers a sustainable alternative to conventional cementitious systems, with lower carbon emissions and improved durability. However, its fracture behaviour received limited attention. This study investigates the influence of Fly Ash (FA) content and Coarse Aggregate (CA) volume on the fracture performance of slag-based AASCC. Fifteen mix designs were developed by partially replacing Ground Granulated Blast Furnace Slag (GGBS) with FA (20%–50% by weight) and varying CA volume from 40% to 60% of total aggregate volume. An OPC-based SCC mix at each volume fraction of CA was developed as a control mix. Beam specimens were tested under three-point bending to evaluate fracture properties using the Work of Fracture Method (WFM) and Size Effect Method (SEM). Fresh and hardened strength properties were first assessed. Fracture energy (G_F) was determined using WFM for all 15 mixes. A 20% FA replacement improved mechanical strength and G_F across all CA volumes at 28 days, outperforming OPC-based SCC and FA-free alkali-activated mixes. Fracture parameters such as fracture toughness (K_{IC}), fracture energy (G_f), effective fracture process zone length (C_f), and critical crack tip opening displacement ($CTOD_c$) were calculated using SEM for five mixes with 40% CA. Results showed the sensitivity of fracture parameters to material variations. Peak values observed were G_f = 46.33 N/m, C_f = 42.33 mm, K_{IC} = 34.44 MPa$\sqrt{mm}$, and $CTOD_c$ = 0.028 mm. The average G_F/G_f ratio was 3.43, indicating consistent scaling behaviour. The G_F/G_f ratio helps to calibrate simplified testing methods for field applications, making fracture-based quality control and performance assessment more accessible. The findings suggest that incorporating 20% FA and 60% CA enhances the fracture performance of AASCC, making it more possible for structural applications requiring high energy absorption and crack resistance.

Major Findings: *Increasing the coarse aggregate (CA) volume from 40% to 60% significantly improves fracture energy (G_F) and characteristic length (L_{ch}) across all fly ash (FA) levels. Replacing GGBS with 20% FA leads to the most significant improvement in fracture energy (G_f), fracture toughness (K_{IC}), and fracture process zone length (C_f), indicating enhanced ductility and toughness. The brittleness number (β) highlights the nonlinear fracture behaviour of AASCC, indicating the need for design based on nonlinear fracture mechanics instead of linear elastic fracture mechanics.*

Keywords: *Alkali Activated Self-Compacting Concrete, Fracture Properties, Size Effect Method (SEM), Work of Fracture Method (WFM)*

1.0 Introduction

With rising awareness of environmental challenges, particularly global warming, the construction industry has been actively pursuing strategies to reduce carbon dioxide (CO_2) emissions and mitigate its ecological footprint. Alkali-Activated Binders (AAB) offer a sustainable alternative to traditional Ordinary Portland

*Author for correspondence

Cement (OPC) by utilising industrial by-products like FA and GGBS[1,2]. AAB can cut carbon emissions by more than 50%, making alkali-activated concrete (AAC) a more sustainable alternative to OPC-concrete and promoting greener construction practices. The AAB forms a strong, durable matrix by activating with alkaline solutions, without the need for high clinker content[3]. They have excellent mechanical properties and chemical resistance, particularly under aggressive environments[4]. Furthermore, when AABs are used to completely replace OPC in concrete, they tend to exhibit enhanced bonding with aggregates, resulting in a stronger ITZ and improved overall microstructure[5].

Alkali-activated systems utilising only FA typically require elevated temperature curing, which presents a significant barrier to widespread adoption in the concrete industry. At the same time, those based exclusively on GGBS are prone to flash setting, reduced workability, and substantial drying shrinkage[6]. To mitigate these issues, this research presents experimental findings on a series of GGBS/FA blends designed to prevent rapid setting and eliminate the need for elevated temperature curing while ensuring favourable fresh, hardened, and fracture properties. Self-Compacting Concrete (SCC) easily fills the formwork, filling complex shapes without mechanical vibration. In this study, this technology is adopted and developed into Alkali-Activated Self-Compacting Concrete (AASCC) to mitigate modern-day on-site construction difficulties.

Despite its many advantages, AAC is inherently brittle. Investigating the fracture properties of AAC mixes is essential to understanding their crack propagation behaviour, which is critical for improving their structural application. Pan *et al.*[7] observed that geopolymer concrete had a characteristic length three times smaller than OPC concrete with a 28% increase in tensile strength, 22% reduction in elastic modulus, and 24% lower fracture energy (G_F), indicating greater brittleness. Ghasemzadeh Mousavinejad and Sammak[8] found that increasing steel fibre content in Ultra-High-Performance Geopolymer Concrete (UHPGC) significantly enhanced G_F and ductility, while partial replacement with polypropylene fibre slightly reduced them. Ding *et al.*[9] reported that slag-based AAC exhibited significantly higher G_F than OPC concrete. Rooholamini *et al.*[10] showed that adding graphite to AAC decreased fracture toughness and G_F. Alzeebaree[11] reported that slag-based AASCC achieved improved G_F and stress intensity factor with 5% metakaolin and up to 2% Nano silica. Kuttagola and Prashanth[12] offering a technically viable and eco-efficient alternative that aligns with global sustainability goals. This study explores optimizing fracture properties in self-compacting alkali-activated concrete (SAAC reported the highest G_F (206.3 N/m) and stress intensity factor (1.91 MPa√m) in self-compacting alkali-activated concrete (SAAC) with 0% FA and 16 mm aggregate size, while 50% FA increased ductility but reduced fracture toughness.

Concrete is a heterogeneous material comprising hardened cement paste, aggregates, and an Interfacial Transition Zone (ITZ) that binds them together[13]. Since aggregates constitute approximately 60-70 % of the total volume of a concrete mix, they are essential in determining the overall characteristics of the concrete. They have a significant influence on both the fresh and hardened properties of concrete, particularly their fracture behaviour[14]. Concrete structures often contain

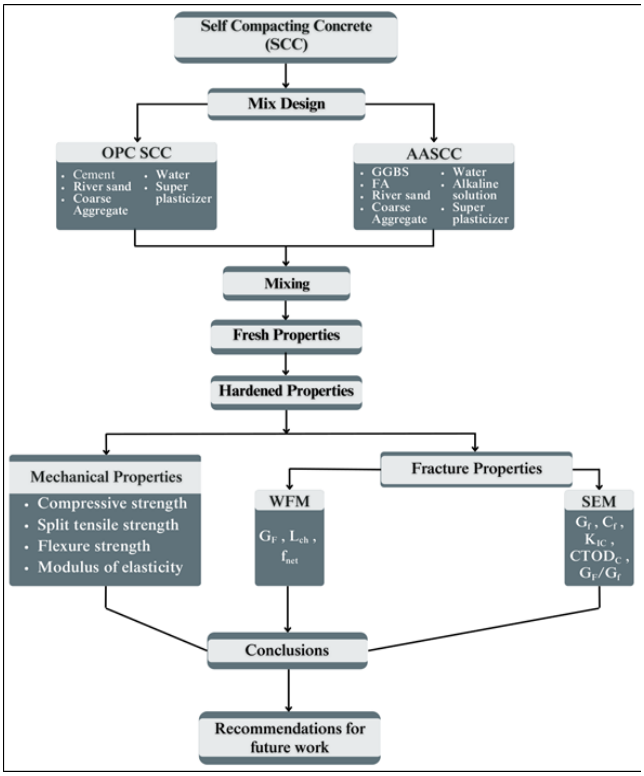


Figure 1. Schematic representation of the research process

inherent defects and microcracks. These act as initiation sites for further cracking and can lead to debonding between aggregate particles and the cement matrix[15]. Under applied loads, these micro-cracks may grow and coalesce into larger, macro-scale cracks, potentially compromising the structural integrity of concrete and visual appearance[16]. Despite this, cracking is a natural characteristic of concrete and does not inherently signify failure; stabilised cracks can be non-critical. To accurately evaluate their impact, a comprehensive understanding of the material's fracture behaviour is essential.

The current literature study shows limited attention is given to the fracture properties of AASCC, especially using the SEM. Although GGBS is increasingly adopted in sustainable concrete systems, its application in SCC has rarely been evaluated from a fracture mechanics perspective under ambient curing. Moreover, existing studies tend to isolate the effects of FA replacement and CA volume, with no research addressing their combined influence on the fracture performance of AASCC. These research gaps highlight the need for a comprehensive study that addresses the synergy of FA and CA content in AASCC and evaluates its fracture properties under ambient curing using standardised fracture testing methods.

2.0 Research Significance

To the best of the author's knowledge, no research has ever explored the combined effect of the GGBS replacement with FA and CA volume variation of the mixes on the fracture properties of AASCC. This work developed a new ambient-cured AASCC, utilising GGBS and FA as binders, activated by alkaline solutions as a complete replacement for OPC in concrete with different CA contents. These variations aim to enhance both mechanical strength and fracture performance. The outcomes offer new insights into the fracture resistance of AASCC under ambient curing conditions, supporting its potential as a sustainable and practical alternative for on-site construction.

The present study explores the combined effect of different volume fractions of CA and FA as replacements for GGBS on the fracture properties of AASCC. In total, 90 notched beams were tested by Three-Point Bending (TPB). Fracture properties, including total fracture energy (G_F), initial fracture energy (G_f), characteristic length (L_{ch}), the effective length of fracture process zone (C_f), and the relationship between $G_F/G_{f,}$ were evaluated by using WFM and SEM.

The flowchart shows clear overview of the research, outlining the key stages of this study.

3.0 Materials and Methodology

3.1 Materials

OPC-53 Grade Cement, following BIS specification IS: 12269-1987[17] with specific gravity–3.13, we used for the control OPC-based SCC mix. The GGBS utilised in this study, obtained from the JSW plant in Bellary, Karnataka, India, complies with IS 12089-2008 specifications. FA conforming to IS 3812-2003[18], sourced from UPCL in Udupi district, Karnataka, India, was used. Table 1 presents the physical and chemical properties of GGBS and FA, with values in brackets representing the corresponding limits specified in relevant Indian Standard (IS) codes. In this investigation, the alkaline activator consisted of a sodium silicate (Na_2SiO_3) solution comprising 32.8% SiO_2, 14.7% Na_2O, and 55.5% H_2O by mass, combined with 98% purity sodium hydroxide (NaOH) pellets. The alkaline activator solution preparation involved dissolving NaOH pellets

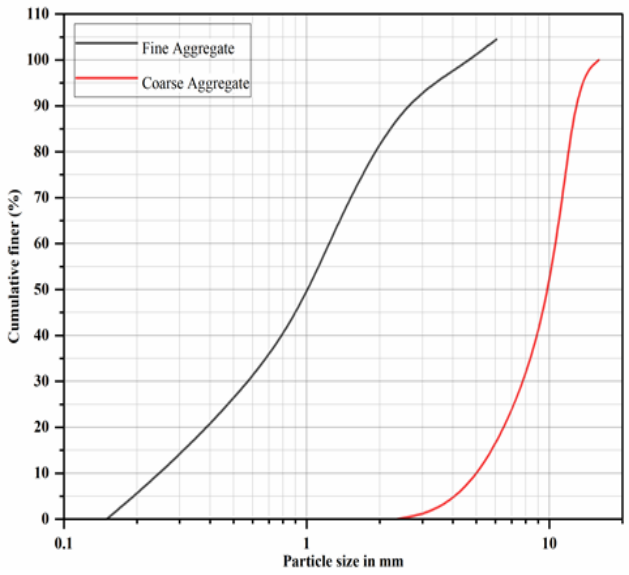


Figure 2. Fine and CA gradation curves.

Table 1. GGBS and FA physicochemical properties

Sl. No	Test	GGBS (IS 12089-2008)	FA (IS 3812- 2003)
Physical properties			
1	Specific gravity	2.90	2.20
2	Blaine's fineness	370(>320)	345(>320)
Chemical properties (Weight Percentages)			
		(%)	(%)
1	CaO	38.63	1.17(<10)
2	Al_2O_3	15.83	34.71
3	Fe_2O_3	0.67	5.46
4	SiO_2	33.88	52.98 (57)
5	MgO	7.35(<17%)	1.55 (5)
6	SO_3	0.31(<5.5%)	0.96(3)
7	Na_2O	0.39 (<2%)	0.87
8	K_2O	1.59	0.32
9	Loss on ignition	1.41	1.6(5)

in potable water, followed by the addition of Na_2SiO_3 solution. The mix underwent thorough stirring to achieve homogeneity, and we subsequently allowed it to cool to ambient temperature to dissipate the heat generated during the exothermic dissolution process. The selection of Na_2SiO_3 and NaOH was based on their accessibility and proven effectiveness in relevant applications[19]. Natural river sand conforming to Zone II we used as the fine aggregate, while crushed Coarse Aggregates (CA) with a maximum size of 12.5 mm were employed in this study. The particle size distribution of both the fine and coarse aggregates is presented in Figure 2, indicating fineness moduli of 2.93 and 7.62, respectively. Potable laboratory water was used for mixing and casting of both OPC and AASCC specimens, as well as for curing the OPC-based SCC specimens.

A new-generation polycarboxylic ether-based superplasticiser, Master Glenium ACE 30 (JP), having a specific gravity of 1.09, a pH greater than six, and a chloride content of less than 0.2%, supplied by M/s BASF Chemicals Bangalore, India, we utilised in this study. It enhances the flow and pumpability of concrete, making it ideal for Self-Compacting Concrete (SCC) and highly workable mixes. The superplasticiser we incorporated at varying dosages based on the total binder content, tailored to achieve the desired workability.

3.2 Methodology

3.2.1 Work of Fracture Method (WFM)

The RILEM 50-FMC introduced WFM, often referred to as Hillerborg's method, which offers the simplest approach to calculate fracture energy (G_F), a crucial fracture property of concrete[20]. The G_F represents the energy needed to propagate a crack per unit surface area. The G_F was determined by performing a TPB test on notched beams, using Equation (1).

$$G_F = \frac{W_0 + mg\delta_0}{b(d - a_0)} \quad (1)$$

where, d and b represent specimen height and width (m), a_0 indicates the depth of notch(m), δ_0 is the final displacement of the beam at failure (m), g refers to gravitational acceleration (9.81 ms^{-2}), m is the specimen mass between the supports (kg), W_0 denotes the area under the load-deflection curve (Nm), and G_F is the total fracture energy of concrete (N/m).

The G_F alone is insufficient to assess the ductility or brittleness of concrete. Alternatively, a material parameter called characteristic length (L_{ch}), as suggested by Hillerborg[21] is used and is defined by Equation (2).

$$L_{ch} = \frac{EG_F}{f_t^2} \quad (2)$$

Where f_t is the net tensile strength, and E is the modulus of elasticity of concrete. In WFM, L_{ch} corresponds to the extension of the cohesive zone during concrete fracture. A higher value of L_{ch} signifies enhanced ductility and greater resistance to crack propagation[22].

3.2.2 Size Effect Method

RILEM TC89-FMC introduced another approach to determine fracture properties independent of specimen size[23]. Based on the Size Effect Law (SEL), proposed by Bazant and Kazemi, this approach offers an alternative to complement and eliminate the disadvantages of WFM[24]. This method, known as the Size Effect Method (SEM), estimates fracture properties by examining the peak loads of different sizes of geometrically similar specimens[25].

Based on the SEL, Bazant and Pfeiffer introduced a general nonlinear equation establishing the relationship between nominal failure stress and specimen size[26].

$$\sigma_N = \frac{B}{\sqrt{1+\beta}} \quad \beta = \frac{d}{d_0} \quad (3)$$

Where σ_N denotes the nominal strength of geometrically similar specimens, B and d_0 are the empirical coefficients associated with material properties and structure geometry, and β is the brittleness number.

According to Equation (3), when β < 0.1, the structural behaviour tends toward a ductile mode, following the strength criterion. For β > 10, the behaviour becomes more brittle, aligning with Linear Elastic Fracture Mechanics (LEFM). The structure follows Nonlinear Elastic Fracture Mechanics (NLFM) in the intermediate range of 0.1 ≤ β ≤ 10.

In this method, to achieve accuracy, a correction for the specimen's load-carrying capacity must be applied to account for the influence of its self-weight.

The corrected peak loads P^0_1,.....P^0_n, are calculated taking the weight of the specimens into account.

$$P^0 = P_j + \frac{2S_j - L_j}{2S_j} m_j g \quad (j=1, 2.\ldots.n) \quad (4)$$

Where n = number of tests conducted, m_j = mass of specimen j, P^0 = corrected peak load, and P_j= measured peak load, g = gravitational acceleration,[27]

Equation (3) can be rewritten to simplify the evaluation of the constants in the Size effect law[28] as

$$\left(\frac{1}{\sigma_N}\right)^2 = \left[\frac{1}{(Bf_t)^2 d_0}\right] d + \left[\frac{1}{(Bf_t)}\right]^2 \quad (5)$$

If the experimental data is plotted, an equation for a linear regression can be obtained in the form Y = AX + C. The slope (A) and intercept (C) of the regression line can be determined from the plot, allowing coefficients B and d_o to be calculated from A and C. Here,

$$X = d \text{ and } Y = \left(\frac{1}{\sigma_N}\right)^2 \quad B = \frac{1}{\sqrt{C}} \quad d_0 = \frac{C}{A} \quad (6)$$

For significantly large specimen sizes, where LEFM is applicable, auxiliary values for extrapolation must be calculated. For known values of relative $\alpha = \frac{a_0}{d}$

$$F_{2.5}(\alpha) = \frac{1 - 2.5\alpha + 4.49\alpha^2 - 3.98\alpha^3 + 1.33\alpha^4}{(1-\alpha)^{3/2}} \quad (7)$$

$$F_4(\alpha) = \frac{1.99 - \alpha(1-\alpha)(2.15 - 3.93\alpha + 2.7\alpha^2)}{\pi \frac{1}{2}(1+2\alpha)(1+2\alpha)^{\frac{3}{2}}} \quad (8)$$

$$F_8(\alpha) = 1.11 - 2.12\alpha + 7.71\alpha^2 - 13.55\alpha^3 + 14.25\alpha^4 \quad (9)$$

Where α = relative crack length, and a_0 is the initial crack length

Linear interpolation is used for other values of S/d. For 4 < S/d <10

$$F(\alpha) = F_4(\alpha) + \frac{[(S/d)-4]}{4}[F_8(\alpha) - F_4(\alpha)] \quad (10)$$

Now, the mean fracture energy G_f and the Effective length of the fracture process zone (C_f) are calculated using the following expressions:

$$G_f = \frac{g(\alpha)}{AE} \quad (11)$$

$$C_f = \frac{g(\alpha)}{g'(\alpha)}\left(\frac{C}{A}\right) \quad (12)$$

Where g(α) is the dimensionless function that defines the structural geometry and is referred to as the dimensionless energy release rate, g'(α) is the derivative of g(α) with respect to the relative initial crack length (α = a_0/d), and a_0 is the initial crack length. The functions g(α) and g'(α) are determined based on LEFM.

Equation (13) gives the g(α) with respect to the span/depth (S/d) ratio as

$$g(\alpha) = \left(\frac{S}{d}\right)^2 \pi\alpha[1.5F(\alpha)]^2 \quad (13)$$

For α = a_0/d, g (α) is to be calculated.

In SEM, the key additional fracture parameters, like the effective crack tip opening displacement (δ_c) and fracture toughness (K_{IC}), are evaluated at peak load.

$$K_{IC} = \sqrt{EG_f} \quad (14)$$

$$\delta_C = \frac{8K_{IC}}{E} \times \sqrt{\frac{c_f}{2\pi}} \quad (15)$$

4.0 Experimental Investigation

4.1 Mix Proportions

A total of fifteen different mixes were analysed to assess the fracture behaviour of AASCC mixes. Among them, twelve were AASCC mixes, designed on a trial basis due to the lack of established guidelines and standards, while the remaining three were the OPC-based SCC control mixes, designed by IS 10262-2019[29]. Table 2 displays the mix compositions of various candidate mixes. FA replacement was incorporated only in the GGBS-based AASCC mixes at 0%, 20%, 35%, and 50% by weight of the total binder content. The volume of CA was varied at 40%, 50%, and 60% relative to the total aggregate volume across all mixes.

In mix designations, Table 2 OPC represents Ordinary Portland Cement, G100 denotes AASCC composed entirely of GGBS, FA20 signifies a mix where 20% of GGBS in G100 is replaced with FA, and V40 indicates a CA volume of 40% with the remaining 60% as fine aggregate.

4.2 Mixing of Concrete Mixes

The normal mixing process was followed to obtain homogeneous OPC-based mixes. The process of mixing the alkali-activated concrete began with placing the required quantity of coarse aggregate and fine aggregate into the pan mixer. Then, FA and GGBS were introduced, and dry mixing continued for three minutes, ensuring uniform mixing. The pre-prepared alkaline activator solution was gradually poured while the mixer remained in operation. After three minutes, superplasticiser with the remaining water was introduced, and mixing we extended for an additional three minutes until a homogeneous mix was achieved[30].

4.3 Fresh State Properties of Concrete Mixes

After mixing, the fresh state properties of the mixes were assessed by slump flow, L-box, and V-funnel tests. The results, presented in Table 2, of all the mixes satisfied the SCC performance criteria of EFNARC[31].

4.4 Casting and Curing of Test Specimens

After testing, fresh concrete was poured into lubricated moulds, without any vibration or compaction, and we subsequently kept it under ambient curing conditions in the laboratory. Standard cube specimens of 100mm×100mm×100mm size for compressive strength, six cylinders of size 150dia×300mm for split tensile strength, and three prism specimens of 100mm×100mm×500mm for flexural strength test,

served to assess hardened strength properties of each mix[32].

To determine the fracture properties using the WFM method, notched beam specimens of size 100 ×100 × 500mm were cast. Geometrically similar notched beams with constant width and in three size variations, small, medium, and large, with dimensions of 262.5 × 75 × 50mm, 525 × 150 × 50 mm, and 1050 × 300 × 50mm, were cast. These specimens were designed to facilitate the evaluation of fracture properties using the SEM. The schematic diagrams representing the specimens in WFM and SEM are presented in Figure 3. The specimen size range is a critical factor influencing the reliability of results obtained using the SEM. A sufficiently wide size range is required to reduce the impact of random scatter of results caused by material heterogeneity and

Table 2. Mix compositions and fresh property characteristics of OPC and alkali-activated-based SCC mixes.

Mix Designations	Mix proportions (kg/m^3)									Fresh properties of mixes		
	OPC	GGBS	FA	Fine Aggregate	CA	SS	SH	Water	SP	Slump flow (mm)	V-funnel flow time (s)	L-box ratio
Series-I (Fine to coarse aggregate volume 60:40)												
OPCV40	650	0	0	812	522	0	0	260	2.0	690	8.50	0.84
G100V40	0	700	0	701	476	149	35	188	3.5	710	7.55	0.84
FA20V40	0	560	140	672	456	149	35	188	3.5	745	7.10	0.88
FA35V40	0	455	245	650	442	149	35	188	2.1	785	6.85	0.89
FA50V40	0	350	350	629	427	149	35	188	2.1	810	6.33	0.95
Series-II (Fine to coarse aggregate volume 50:50)												
OPCV50	650	0	0	677	690	0	0	260	2.0	705	7.70	0.82
G100V50	0	700	0	584	595	149	35	188	3.5	725	7.10	0.81
FA20V50	0	560	140	560	571	149	35	188	3.5	760	6.80	0.86
FA35V50	0	455	245	542	552	149	35	188	2.1	785	6.60	0.85
FA50V50	0	350	350	524	534	149	35	188	2.1	825	6.20	0.91
Series-III (Fine to coarse aggregate volume 40:60)												
OPCV60	650	0	0	541	828	0	0	260	2.0	745	7.00	0.81
G100V60	0	700	0	467	714	149	35	188	3.5	770	6.90	0.80
FA20V60	0	560	140	448	685	149	35	188	3.5	790	6.35	0.83
FA35V60	0	455	245	434	663	149	35	188	2.1	805	6.20	0.81
FA50V60	0	350	350	419	641	149	35	188	2.1	845	6.10	0.89

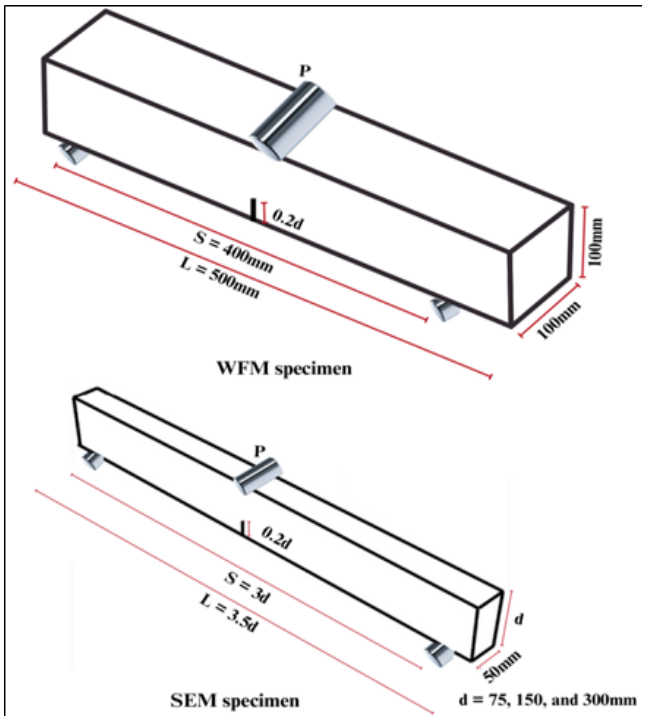


Figure 3. Schematic views of beam specimens under various fracture evaluation approaches.



Figure 4. Geometry of SEM specimens for the TPB test.

measurement uncertainties. A minimum size ratio of 1:4 is commonly recommended in the literature to ensure statistical robustness, and is adopted in the present study. Figure 4 presents a representative set of beam specimens prepared for TPB tests to assess fracture properties using SEM.

After a day of casting, the demoulded AASCC specimens were subjected to ambient curing in the laboratory until the age of testing, and the OPC mix specimens were cured in water until their designated testing age.

4.5 Three-Point Bending (TPB) Test

Three-Point Bending (TPB) tests were conducted on



Figure 5. Experimental Test setup

notched beam specimens. Each specimen was pre-cut with a central notch measuring 3 mm in width. The beams were simply supported with the notched face facing downward, following the specifications for WFM and SEM specimens. Three identical specimens were prepared for each test.

A 100 kN servo-controlled closed-loop universal testing system performed TPB tests of all beam specimens under displacement-controlled loading. The loading rates were adjusted to ensure that the peak load was attained within one minute for specimens tested under WFM and within five minutes for those tested under SEM, respectively. A clip gauge mounted at the mouth of the notch was used to measure the Crack Mouth Opening Displacement (CMOD). All tests were conducted under displacement control at a constant displacement rate in each method[33]. The load–midspan deflection (P–δ) and load–crack mouth opening displacement (P–CMOD) curves and the data of the tested beams were recorded. The experimental setup for the TPB tests is illustrated in Figure 5.

5.0 Experimental Results and Discussion

This paper primarily focuses on the fracture properties of AASCC; the detailed discussion of its fresh and hardened strength properties is not included. However, the key experimental results, including compressive strength (f_c), net tensile strength (f_{net}), and modulus of elasticity (E) of all the mixes, are summarised in Table 3.

Table 3. Fracture properties of OPC-SCC and AASCC using WFM

Mix Designations	f_c (MPa)	f_t (MPa)	f_{net} (MPa)	E (GPa)	G_F (Average) (N/m)	L_{ch} (mm)
Series-I (Fine to coarse aggregate volume 60:40)						
OPCV40	68.67	3.80	2.39	30.15	130.27	272.0
G100V40	79.00	3.57	2.32	26.04	137.60	281.1
FA20V40	75.00	3.72	2.30	25.60	148.07	273.8
FA35V40	76.67	3.75	1.91	24.90	139.98	247.4
FA50V40	67.33	3.43	2.14	24.60	131.50	274.2
Series-II (Fine to coarse aggregate volume 50:50)						
OPCV50	64.67	3.75	2.45	32.15	144.77	331.0
G100V50	75.00	3.61	2.25	27.41	145.22	305.1
FA20V50	73.33	3.77	2.06	26.74	159.95	301.3
FA35V50	71.33	3.48	2.07	26.30	141.91	308.9
FA50V50	65.00	3.43	1.89	25.89	138.58	304.1
Series-III (Fine to coarse aggregate volume 40:60)						
OPCV60	65.33	3.65	2.60	33.65	149.92	378.7
G100V60	74.33	3.55	2.39	28.25	159.00	356.1
FA20V60	75.33	3.66	2.16	27.22	170.65	346.9
FA35V60	66.67	3.52	1.93	28.10	150.94	341.7
FA50V60	64.00	3.34	2.13	26.93	149.93	361.2

5.1 Load-CMOD and Load-Deflection Responses

Typical experimental P-CMOD and P–δ responses for OPCSCC and FA20 (AASCC) specimens with varying CA volume percentages are shown in Figures 6 and 7. The P–δ response of mixes with varying aggregate volume fractions (V40, V50, and V60) shows that increasing CA content enhances peak load capacity. After an initial linear response, cracking initiates and the peak load is reached quickly[34]. In post-peak, lower CA mixes exhibit sharp load drops, indicating brittle failure, while V60 demonstrates a more gradual decline, reflecting improved post-peak behaviour, energy absorption, and fracture resistance. This highlights the role of aggregates in enhancing toughness and effective load transfer during crack propagation.

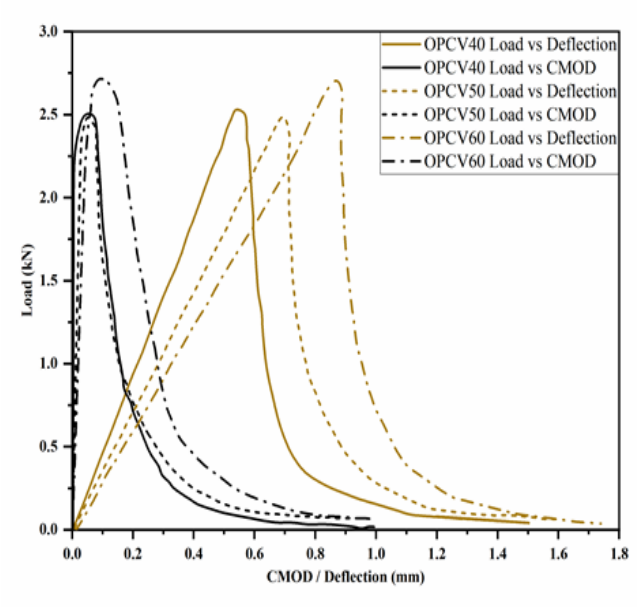


Figure 6. Load-CMOD and Load-deflection curves of OPC specimens with different volume percentages of CA.

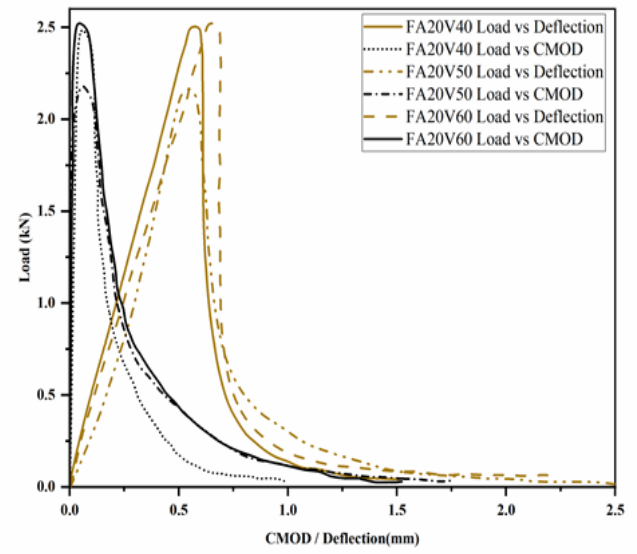


Figure 7. Load-CMOD and Load-deflection curves of AASCC (FA20) specimens with varying volume percentages of CA.

All mixes exhibited an initial elastic phase followed by strain softening beyond the peak load[35]. As aggregate volume increases, both peak load and post-peak ductility improve. V60 mixes show higher resistance to cracking, more gradual softening, and greater energy absorption, attributed to better aggregate interlock and crack bridging. In contrast, lower CA content (V40) showed steeper post-peak softening and more brittle failure response.

5.2 Fracture Properties Assessment Using WFM

5.2.1 Influence of FA and CA Volume on Fracture Energy (G_F)

Figure 8 shows the influence of FA and CA on the G_F of AASCC mixes. Incorporating FA in AASCC with constant CA leads to a notable reduction in G_F. This reduction is primarily attributed to the lower calcium content in FA, which results in a less dense binder matrix and a weaker Interfacial Transition Zone (ITZ), thereby diminishing resistance to crack propagation[36]. Mixes with higher FA content exhibit more brittle post-peak behaviour, with steeper load drops and reduced energy absorption capacity. This is attributed to the slower strength development, delayed pozzolanic activity of FA and due to the presence of larger unhydrated particles, which act as flaws within the matrix and hinder effective stress transfer[37]. Mixes with low FA content exhibited higher fracture energy, making them more suitable for structural applications. The average G_F values are presented in Table 3. The 20% FA replacement level demonstrated the best overall performance, balancing workability, mechanical strength, and fracture characteristics.

However, the increase in CA volume in OPCSCC, GGBS, and GGBS–FA modified AASCC mixes has

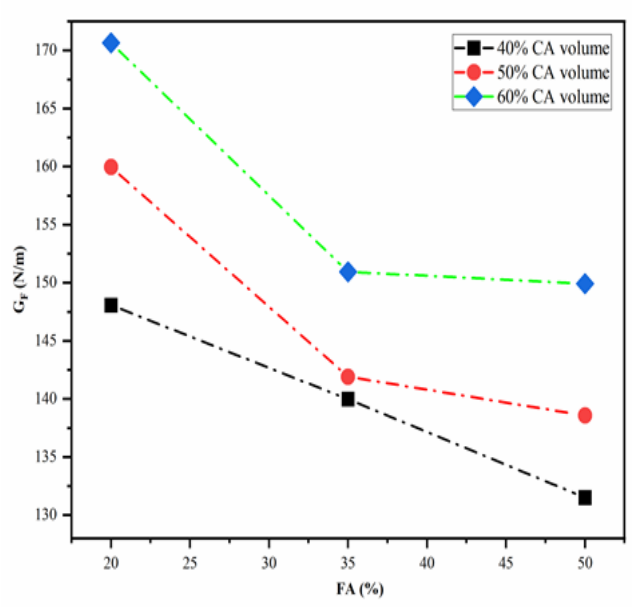


Figure 8. FA Percentage versus Fracture Energy (G_F).

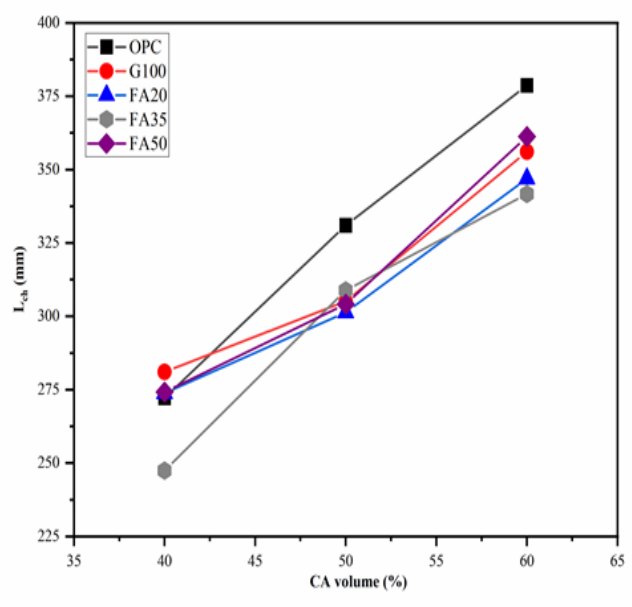


Figure 9. Lch with a coarse aggregate volume.

shown an increase in G_F. This enhancement is primarily attributed to the expansion of the Fracture Process Zone (FPZ) with higher aggregate content, which promotes micro-cracking and improves overall fracture resistance[38]. The improvement in fracture performance can be further ascribed to enhanced crack-bridging, increased tortuosity of the fracture path, and improved mechanical interlock between aggregates and the matrix. These factors collectively contribute to greater energy dissipation during fracture. The total G_F increases from 148.07 N/m (FA20V40) to 170.65 N/m (FA20V60) when the CA volume increases from 40% to 60%. An overall 15.25% increase in G_F (FA20) was observed in the present study, which agrees with previous studies[39]. This suggests that a higher CA content can enhance fracture performance, even in mixes exhibiting delayed strength gain.

5.2.2 Effect of FA and CA Volume Variation on L_{ch}

Figure 9 illustrates the influence of FA and CA volume on the L_{ch} of concrete mixes. The average L_{ch} values are summarised in Table 3. The results demonstrate that the average L_{ch} values of AASCC mixes increased from 281.1 mm to 361.2 mm, while in OPC-SCC mixes, it improved from 272 mm to 378.7 mm as the CA volume increased from 40% to 60%. These trends are attributed to both microstructural and fracture mechanics phenomena[40]. Here, increased CA volume promotes matrix–aggregate debonding and crack path tortuosity, enhancing energy dissipation. Also, optimal FA content improves pore structure, densifies the matrix, and strengthens the ITZ, leading to shorter crack lengths and improved toughness[41]. However, excessive incorporation of FA weakens the binder matrix and diminishes crack resistance. The results indicate that an FA replacement level in the range of 20-50 % is suitable for enhancing the L_{ch} of AASCC.

5.2.3 Fracture Surface of Specimens

Figure 10 illustrates the fractured surface for a 40% CA volume. Generally, the AASCC specimens exhibited a more brittle failure mode compared to the OPC concrete specimens[42]. Typical fracture failure planes of AASCC and OPC concrete specimens are shown in Figure 10. It can be observed that the fracture planes in OPC concrete were more tortuous, whereas those in AASCC specimens appeared relatively smooth. Despite both concretes having similar compressive strengths, in OPC concrete, the fracture planes were observed to pass around the aggregates, while in AASCC, they commonly passed through the aggregates. This distinction is clearly

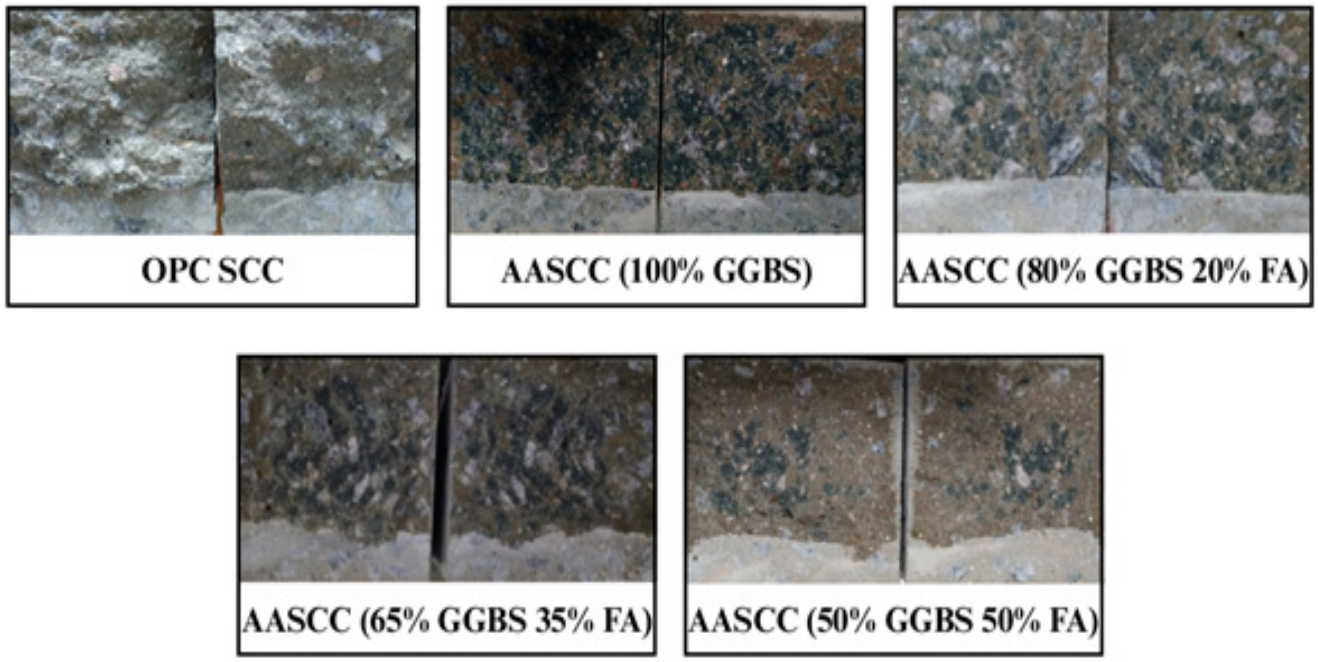


Figure 10. Fracture surface of specimens.

illustrated in Figure 10. The tendency for fracture planes to pass through the aggregates in AASCC is attributed to the higher bond strength between the alkali-activated binder and the aggregates, in comparison to the OPC matrix. Previous studies have also shown that alkali-activated systems demonstrate stronger bonding than OPC concrete[43].

OPC concrete shows a fracture surface influenced by the dual role of aggregates, which act both as toughening agents and potential weak points. The resulting fracture morphology reflects the combined effects of the matrix microstructure and the interfacial bond strength between the aggregates and the cementitious matrix. GGBS concrete exhibits rough, micro-cracked surfaces with visible aggregate pull-out, where fractures propagate around aggregates. Blended with FA inclusion (80/20, 65/35,50/50) displays smoother, denser, and finer fracture surfaces, indicating improved microstructure, bonding, and reduced microcracking. These features lead to increased toughness, durability, and fracture resistance, with pozzolanic activity and aggregate interaction playing key roles in enhancing the structural resilience of these blended concrete mixes.

5.3 Fracture Properties Analysed Using SEM

The SEM is advantageous due to its conceptual simplicity and minimal experimental requirements. TPB tests are conducted on geometrically similar notched beams of series-I mixes. To ensure the reliability of the results, the recorded peak loads must be corrected to account for the influence of the specimen's self-weight. This correction is performed using Equation (4) to account for the additional load contribution from the specimen's self-weight, ensuring accurate characterisation of the peak load.

Table 4 shows the corrected peak loads of SEM specimens. Equation (6) was employed to perform a linear regression analysis on the corrected peak load values. Table 5 presents the resulting slope (A) and intercept (C) of the regression lines for each mix, along with the corresponding values of ω_A, ω_C, and m. Figure 11 presents the linear regression analysis results for the mix FA50V40 from which the values of A = 0.015 mm^{-1} MPa^{-2} and C = 2.408 MPa^{-2} were obtained. RILEM-TC 89 suggests that the relative width of the scattering band (m) and the slope

Table 4. Corrected peak loads for Series-I mixes

Mix	f_c N/mm²	a_0/d	Depth (d)	Corrected peak loads P⁰(N)			Coefficient of variation (%)
			mm	Beam-1	Beam-2	Beam-3	
OPCV40	68.67	0.20	75	1998	2148	2048	3.70
			150	3605	3405	3705	4.28
			300	5756	6056	6006	2.71
G100V40	79.00	0.20	75	1901	2026	2001	3.35
			150	3493	3593	3543	1.41
			300	5669	5769	5894	1.95
FA20V40	75.00	0.20	75	2147	2147	2087	1.63
			150	3588	3888	3688	4.10
			300	6057	6257	6157	1.62
FA35V40	76.67	0.20	75	2083	1983	2062	2.58
			150	3365	3200	3240	2.63
			300	5360	5660	5757	3.70
FA50V40	67.33	0.20	75	1812	1862	1937	3.36
			150	3305	3432	3525	3.23
			300	5418	5718	5538	2.72

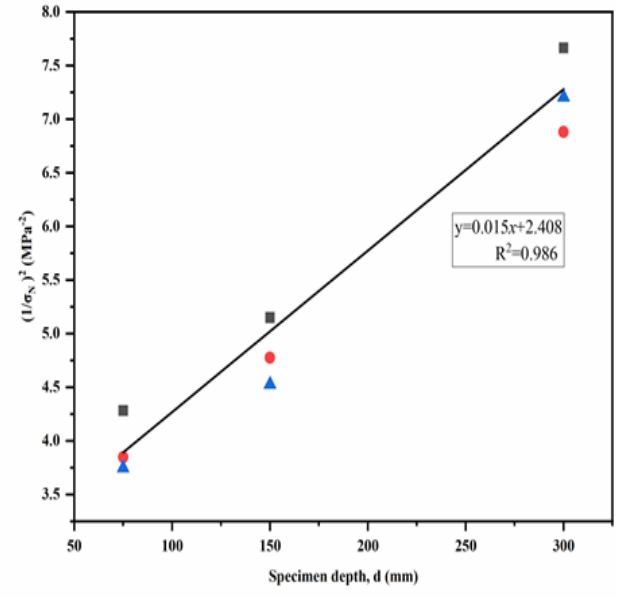


Figure 11. Linear regression for mix FA50V40.

(ω_A) and intercept (ω_C) variation coefficients should not exceed 0.2, 0.1, and 0.2, respectively. In this research, all values satisfied these conditions.

Equations (11)-(15) are utilised to calculate initial fracture energy (G_f), the effective length of the fracture process zone (C_f), K_{IC}, and $CTOD_C$ using the Size effect method, and the values are presented in Table 6.

5.3.1 Effect of FA on Initial Fracture Energy (G_f)

Figure 12 illustrates the change in G_f across various FA substitution levels in Series-I mixes. The results indicate a decreasing trend in the G_f as the FA replacement level increases from 20% to 50%. Notably, incorporating 20% FA into the AASCC mixes led to a 27.60% and 18.67% increase in G_f compared to the plain OPC-based control concrete mix (OPCV40) and the GGBS-based AASCC mixes, respectively.

Table 5. Statistical results from the Regression analysis for the Series-I SCC mixes

Mix Id	A	C	R^2	ω_A	ω_C	M
OPCV40	0.013	2.281	0.993	0.071	0.025	0.097
G100V40	0.014	2.514	0.999	0.089	0.031	0.125
FA20V40	0.012	2.328	0.990	0.075	0.024	0.102
FA35V40	0.014	2.593	0.916	0.064	0.022	0.083
FA50V40	0.015	2.408	0.986	0.091	0.036	0.126

Table 6. Fracture parameters from SEM for series-I mixes

Mix	f_c (MPa)	E (GPa)	f_t (MPa)	a_0/d	$F_{3.0(\alpha_0)}$	$g(\alpha_0)$	G_f (N/m)	C_f (mm)	K_{IC} (MPa·mm$^{1/2}$)	$CTOD_c$ (mm)	B (MPa)	d_0 (mm)
OPCV40	68.67	30.15	3.80	0.2	0.9771	14.23	36.31	38.25	33.09	0.0216	0.662	175.46
G100V40	79.00	26.04	3.57	0.2	0.9771	14.23	39.04	39.14	31.88	0.0244	0.631	179.57
FA20V40	75.00	25.60	3.72	0.2	0.9771	14.23	46.33	42.29	34.44	0.0279	0.655	194.00
FA35V40	76.67	24.90	3.75	0.2	0.9771	14.23	40.82	40.37	31.88	0.0260	0.621	185.21
FA50V40	67.33	24.60	3.43	0.2	0.9771	14.23	38.57	34.99	30.80	0.0236	0.644	160.53

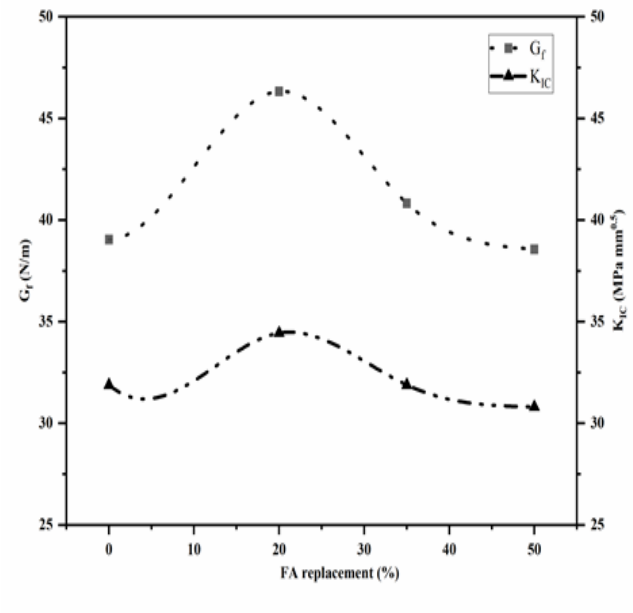


Figure 12. Initial fracture Energy (G_f) and Fracture Toughness (KIC) as a function of FA Substitution Level.

The increase in G_f of AASCC at 20% FA replacement is attributed to the optimal synergy between high-calcium GGBS and low-calcium FA. This balance favours the formation of dense and cohesive C-A-S-H gel, with minor N-A-S-H contributions, enhancing matrix toughness and crack resistance[44]. Improved packing and workability at this level also lead to better compaction and microstructural refinement. However, beyond 20% FA, reduced calcium availability shifts gel formation towards weaker N-A-S-H, while lower FA reactivity and increased porosity degrade the matrix and Interfacial Transition Zone (ITZ), resulting in decreased G_f[45].

5.3.2 Effect of FA on Fracture Toughness (K_{IC})

The results demonstrate that the fracture parameters, K_{IC} and G_f, respond differently to variations in material characteristics. The K_{IC} of AASCC decreases as the percentage of FA increases from 20 to 50 per cent (Figure 12). The highest K_{IC} of 34.44 MPa√mm was observed for the FA20V40 mix, which included 20% FA. The use

of 20 per cent FA replacement led to a 4.08 per cent increase in K_{IC}, while the addition of 35 and 50 per cent FA caused the K_{IC} to decrease by 3.64 and 6.91 per cent, respectively, concerning the control SCC mix based on OPC without FA. Concerning GGBS-only based control AASCC, the K_{IC} increased by 8.01 per cent with 20 per cent FA replacement, but the addition of 50 per cent FA resulted in a 3.39 per cent decrease in K_{IC}, endorsing that the increase in strength development is gradual over age in GGBS-based concrete mixes with higher FA replacement.

FA exhibits a complex relationship with fracture toughness. In early ages, only low volumes of FA may enhance the interfacial bond, whereas high-volume FA AASCC mixes require extended curing periods to achieve similar interfacial bond development. Since K_{IC} represents a local toughness parameter and is primarily influenced by the tensile properties of concrete, prolonged curing has a positive effect on K_{IC} in high-volume fly ash systems. Similar trends were observed in the studies by Lam *et al*[46].

The high-volume fly ash cement paste behaves as a multiphase composite, where unreacted fly ash particles act as stiff micro-aggregates that resist crack propagation. Microcracking around these particles increases energy dissipation, leading to a more nonlinear fracture process and improved toughness.

5.3.3 *Effective Length of Fracture Process Zone (C_f)*

Figure 13 illustrates the variation in the C_f with different levels of FA replacement. As FA content increases from 0% to 20%, C_f reaches a peak of 42.23 mm, indicating enhanced ductility. However, further increases in FA to 35% and 50% reduce C_f to 40.32 mm and 34.94 mm, respectively, suggesting a decline in ductility at higher FA contents. This trend is attributed to changes in the pore structure and the quality of the Interfacial Transition Zone (ITZ), as excessive FA may hinder early-age reaction kinetics and densification. A similar trend was observed by Molaei Raisi *et al.*[47] with other supplementary cementitious materials with varying percentages of replacements in different types of concrete.

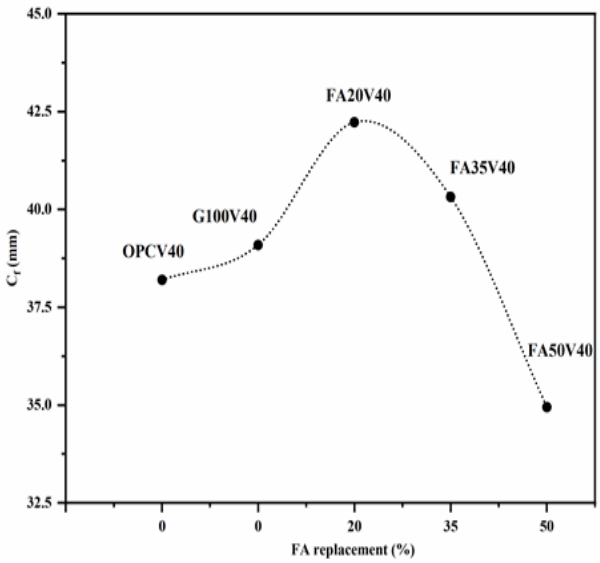


Figure 13. Variation of C_f with FA replacement percent.

5.3.4 *Experimental Peak Loads with those Predicted by SEM*

Figure 14 compares the experimental peak loads with those predicted by SEM, based on the fracture properties calculated in this study. The findings indicate that the

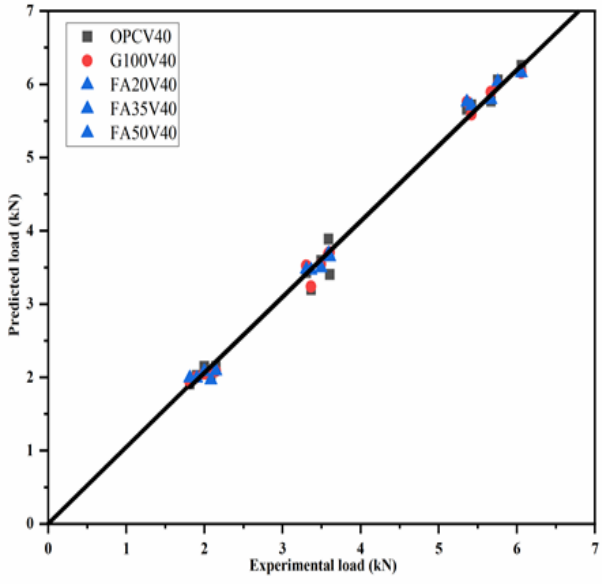


Figure 14. Experimental versus predicted peak loads.

estimated failure loads of SCC mixes align closely with experimental results, demonstrating good agreement and validating the applicability of SEM in capturing the fracture behaviour of AASCC.

5.3.5 Size Effect Plot for Mixes at Different FA Replacement Levels

Figure 15 presents the size effect curve, which closely matches the experimental data. Based on the SEL, a strong correlation exists between the experimental and the predicted load values. As shown in the figure, a rise in the FA ratio affects the specimen's behaviour and changes it towards nonlinear fracture mechanics. This shift is attributed to the enlargement of the FPZ dimensions as the FA content in the mix increases.

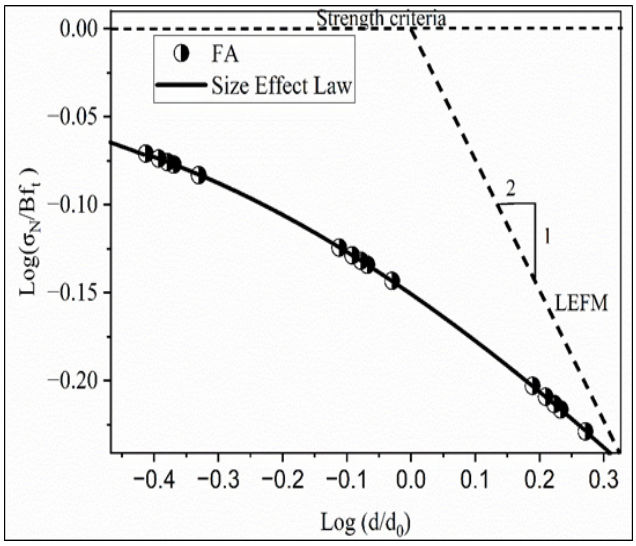


Figure 15. Size effect plot for mixes at different FA replacement levels.

5.3.6 Brittleness Number and Crack Tip Opening Displacement (CTODc)

Figure 16 depicts the relationship between β and beam depth across all the mixes with varying FA replacement levels. The β values for all mixes are consistent with the range commonly seen in nonlinear fracture mechanics ($0.1 < \beta < 10$). Therefore, this indicates that applying either strength-based design or LEFM to AASCC structures may lead to inaccurate results. The incorporation of FA to GGBS in concrete typically results in an increased

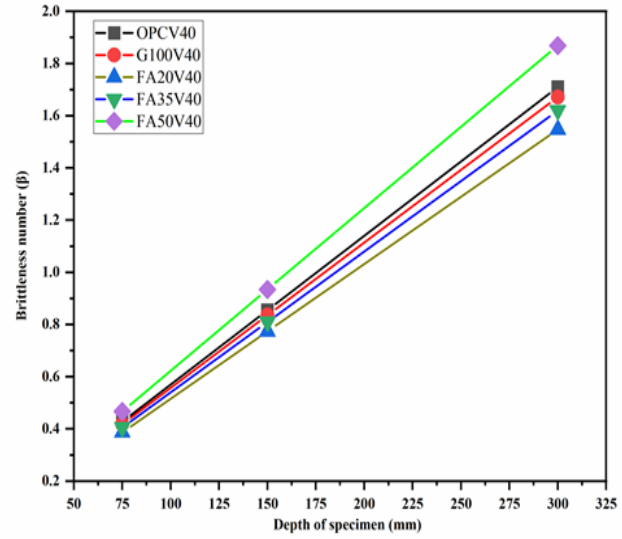


Figure 16. Brittleness number versus beam depth.

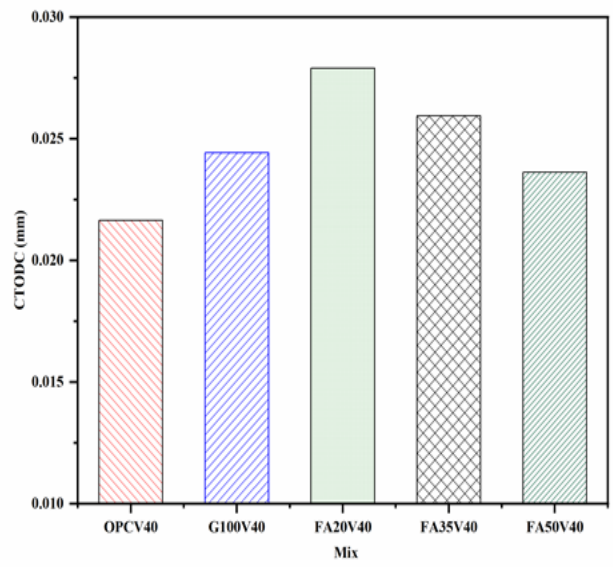


Figure 17. CTODC ratios of all mixes of series-I.

brittleness number (β). This effect is attributed to the synergistic densification of the microstructure caused by FA and GGBS, which can reduce the concrete's overall ductility and toughness[48].

Crack Tip Opening Displacement ($CTOD_C$) is an important parameter in fracture mechanics, representing the crack opening at its tip under stress[49]. Higher $CTOD_C$ values indicate greater fracture toughness, as the material

can withstand larger crack openings before failure. Figure 17 illustrates the variation of $CTOD_C$ with the FA percentage in the Series-I mixes. It illustrates a decrease in $CTOD_C$ with an increase in FA content. The highest $CTOD_C$ value was observed in the FA20V40 mix, which is an AASCC mix. At 20% FA content, the $CTOD_C$ increases by 16%, compared to the control OPC-based SCC mix. In the case of the control GGBS-based AASCC, the $CTOD_C$ increases by 14.41% and 6.40% with 20 and 35 % FA content, respectively, but decreases by 3.12% at 50% FA content. Overall, moderate FA content improves fracture resistance by enhancing the microstructure and promoting crack bridging, whereas excessive replacement reduces fracture toughness due to increased porosity, diminished matrix cohesion, and greater micro-cracking.

5.3.7 Correlation of Fracture Energies Measured by Different Approaches

The calculation of G_F suffers from high uncertainty related to accurately measuring the area under the entire load-deflection curve, particularly at the tail of the post-peak load-deflection curve[50]. Figure 18 illustrates that the mixes in this study exhibited an average G_F/G_f ratio of 3.43, with a coefficient of variation of 3.21 per cent. It was noted that G_F (determined using WFM) and G_f (obtained from SEM) represent distinct characteristics of a concrete mix, with G_f consistently lower than G_F. G_f represents the area under the initial slope of the load-deflection curve of concrete.

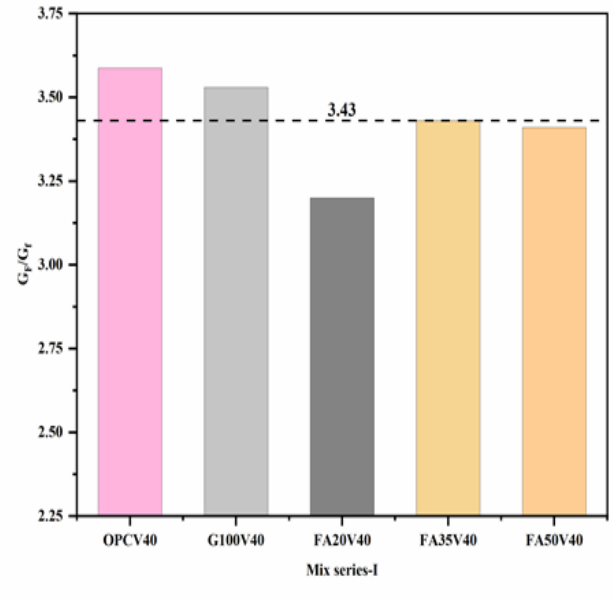


Figure 18. Ratios of GF/Gf of series-I mixes.

6.0 Conclusions

This experimental study investigates the fresh, mechanical strength, and fracture performance of ambient-cured Alkali-Activated Self-Compacting Concrete (AASCC) mixes designed for practical field applications. The research incorporates partial replacement of low-calcium FA and examines the influence of varying CA volumes within GGBS-based AASCC. Fracture properties were systematically evaluated through WFM following RILEM recommendations, including load-displacement response, characteristic length, and fracture energy. Additionally, the SEM was applied to analyse fracture properties and to assess size-independent behaviour, offering deeper insights into the fracture mechanisms and performance of the mixes.

From the experimental observations, the key findings are summarised as follows.

- The change in volume of CA from 40 to 60 per cent significantly enhances G_F and L_{ch}, in AASCC mixes across all FA levels, indicating a more tortuous crack path resulting from improved aggregate interlocking and bridging.
- The G_F increases from 148.07 N/m to 170.65 N/m when aggregate volume increases from 40% to 60% and an overall 15.25% increase in G_F was observed in the (FA20V60) mix compared to control concrete.
- Incorporating 20% FA into the AASCC mixes led to a 27.60% and 18.67% increase in G_f compared to the plain OPC-based control concrete mix (OPCV40) and the GGBS-based AASCC mix.
- The 20 per cent FA replacement led to a 4.08 per cent increase in K_{IC}, while the addition of 35 and 50 per cent FA caused the K_{IC} to decrease by 3.64 and 6.91 per cent, respectively, concerning the control SCC mix based on OPC without FA.
- The effective length of the fracture process zone (C_f) reached 42.23 mm with 20 per cent FA replacement, a 10.57% increase when compared

to the control FA-free SCC mix based on OPC and decreases with higher FA content, indicating reduced ductility.

- The brittleness number (β) values indicate that the design for AASCC members should be solely based on nonlinear fracture mechanics criteria.
- Crack Tip Opening Displacement ($CTOD_C$) decreases with higher FA levels, with the FA20V40 mix showing the highest $CTOD_C$ an increase of 15.41%.
- The G_F/G_f ratio across the mixes averaged 3.43 with a coefficient of variation of 3.21%.
- The fracture planes in the AASCC specimens were less tortuous than those in OPC concrete, indicating a more direct crack propagation path and correspondingly more brittle failure behaviour.

The enhanced fracture toughness of AASCC, achieved by optimising fly ash and coarse aggregate proportions, improves energy dissipation and ductility, making it ideal for seismic applications. Tailored AASCC mixes also offer superior durability and reduced maintenance in precast, long-span, and cast-in-situ elements due to their good performance under ambient curing conditions and better control of microcracking. Additionally, the self-compacting nature combined with increased fracture resistance supports advanced construction methods like slip-forming, enabling the production of complex, high-performance components with excellent crack resistance and dimensional stability.

7.0 References

1. Sherwani AFH, Younis KH, Arndt RW, Pilakoutas K. Performance of self-compacted geopolymer concrete containing fly ash and slag as binders. Sustainability. 2022; 14(22):15063. https://doi.org/10.3390/su142215063
2. Manjunath R, Narasimhan MC. An experimental investigation on self-compacting alkali-activated slag concrete mixes. J Build Eng. 2018; 17:112. https://doi.org/10.1016/j.jobe.2018.01.009
3. Li G, Tan H, Zhang J, Deng X, Liu X, Luo Z. Ground granulated blast-furnace slag/fly ash blends activated by sodium carbonate at ambient temperature. Constr Build Mater. 2021; 291:123378. https://doi.org/10.1016/j.conbuildmat.2021.123378
4. Parhi SK, Nanda A, Panigrahi SK. Multi-objective optimisation and prediction of strength along with durability in acid-resistant self-compacting alkali-activated concrete. Constr Build Mater. 2024; 456:139235. https://doi.org/10.1016/j.conbuildmat.2024.139235
5. Panda S, Panigrahi SK. Production of sustainable GGBFS-based self-compacting geopolymer concrete containing E-waste aggregates under ambient temperature curing. Constr Build Mater. 2024; 440:137373. https://doi.org/10.1016/j.conbuildmat.2024.137373
6. Humad AM, Kothari A, Provis JL, Cwirzen A. The effect of blast furnace slag/fly ash ratio on setting, strength, and shrinkage of alkali-activated pastes and concretes. Front Mater. 2019; 6:1-10. https://doi.org/10.3389/fmats.2019.00009
7. Pan Z, Sanjayan JG, Rangan BV. Fracture properties of geopolymer paste and concrete. Mag Concr Res. 2011; 63(10):763-71. https://doi.org/10.1680/macr.2011.63.10.763
8. Ghasemzadeh Mousavinejad SH, Sammak M. An assessment of the fracture parameters of Ultra-High-Performance Fibre-Reinforced Geopolymer Concrete (UHPFRGC): The application of work of fracture and size effect methods. Theor Appl Fract Mech. 2022; 117:103157. https://doi.org/10.1016/j.tafmec.2021.103157
9. Ding Y, Bai YL. Fracture properties and softening curves of steel fibre-reinforced slag-based geopolymer mortar and concrete. Materials. 2018; 11(8):2104. https://doi.org/10.3390/ma11081445
10. Rooholamini H, Bayat A, Kazemian F. Mechanical and fracture properties of alkali activated concrete containing different pozzolanic materials. Road Mater Pavement Des. 2022; 23(4):802-21. https://doi.org/10.1080/14680629.2020.1845783
11. Alzeebaree R. Bond strength and fracture toughness of alkali activated self-compacting concrete incorporating metakaolin or nanosilica. Sustainability. 2022; 14(11):6798. https://doi.org/10.3390/su14116798
12. Kuttagola I, Prashanth MH. Application of Taguchi's optimisation techniques for enhancing the fracture characteristics and brittleness of self-compacting alkali-activated concrete. Theor Appl Fract Mech. 2025; 138:104931. https://doi.org/10.1016/j.tafmec.2025.104931
13. Tasdemir MA, Karihaloo BL. Effect of aggregate volume fraction on the fracture parameters of concrete: A meso-mechanical approach. Mag Concr

Res. 2001; 53(6):405-15. https://doi.org/10.1680/macr.2001.53.6.405
14. Akcay B, Agar-Ozbek AS, Bayramov F, Atahan HN, Sengul C, Tasdemir MA. Interpretation of aggregate volume fraction effects on fracture behaviour of concrete. Constr Build Mater. 2012; 28(1):437-43. https://doi.org/10.1016/j.conbuildmat.2011.08.080
15. Lee NK, Lee HK. Setting and mechanical properties of alkali-activated fly ash/slag concrete manufactured at room temperature. Constr Build Mater. 2013; 47:1201-9. https://doi.org/10.1016/j.conbuildmat.2013.05.107
16. Korte S, Boel V, De Corte W, De Schutter G. Fracture behaviour of self-compacting concrete compared to vibrated concrete. Pro 90. 2013; 317-24.
17. Bureau of Indian Standards. IS 12269: Ordinary Portland Cement, 53 grade specification. New Delhi: BIS; 2013.
18. Bureau of Indian Standards. IS 3812 (Part-2): Specification for pulverised fuel ash for use as admixture in cement mortar and concrete. New Delhi: BIS; 2003.
19. Thapa S, Debnath S, Kulkarni S, Solanki H, Nath S. Mechanical properties of geopolymer concrete incorporating supplementary cementitious materials as binding agents. Discov Civil Eng. 2024. https://doi.org/10.1007/s44290-024-00064-0
20. RILEM FMC-50. Determination of the fracture energy of mortar and concrete by means of three-point bend tests on notched beams. Mater Struct. 1985; 18(106):287-90. https://doi.org/10.1007/BF02472918
21. Hillerborg A, Modeer M, Petersson PE. Analysis of crack formation and crack growth in concrete by means of fracture mechanics and finite elements. ACI Spec Publ. 2008; SP-249:225-37.
22. Sadrmomtazi A, Lotfi-omran O, Nikbin IM. Influence of cement content and maximum aggregate size on the fracture parameters of magnetite concrete using WFM, SEM and BEM. Theor Appl Fract Mech. 2020; 107:102482. https://doi.org/10.1016/j.tafmec.2020.102482
23. Bazant ZP, Pfeiffer PA. Determination of fracture energy from size effect and brittleness number. ACI Mater J. 1987; 84(6):463-80. https://doi.org/10.14359/2526
24. Salehi H, Mazloom M. An experimental investigation on fracture parameters and brittleness of self-compacting lightweight concrete containing magnetic field-treated water. Arch Civ Mech Eng. 2019; 19:803-19. https://doi.org/10.1016/j.acme.2018.10.008
25. RILEM TC-89. Size-effect method for determining fracture energy and process zone size of concrete. Mater Struct. 1991; 23(6):461-8. https://doi.org/10.1007/BF02472030
26. Bazant ZP. Size effect on structural strength: a review. Arch Appl Mech. 1999; 69(9):703-25. https://doi.org/10.1007/s004190050252
27. Muralidhara Rao T, Gunneswara Rao TD. Size effect of plain concrete beams: an experimental study. Int J Res Eng Technol. 2013; 2(8):1047-55. https://doi.org/10.15623/ijret.2013.0206023
28. Muralidhara Rao T, Gunneswara Rao TD. Fracture parameters of high-strength concrete - an experimental study. J Struct Eng (Madras). 2009; 35(5):397-403.
29. Bureau of Indian Standards. IS 10262:2019 - Concrete Mix Proportioning - Guidelines (Second Revision). New Delhi: BIS; 2019.
30. Sajjad U, Sheikh MN, Hadi MNS. Incorporation of graphene in slag-fly ash-based alkali-activated concrete. Constr Build Mater. 2022; 322:126417. https://doi.org/10.1016/j.conbuildmat.2022.126417
31. EFNARC. Specification and guidelines for self-compacting concrete. European Federation for Specialist Construction Chemicals and Concrete Systems; 2002.
32. Bureau of Indian Standards. IS 516: Method of Tests for Strength of Concrete. New Delhi: BIS; 1959.
33. Bharatkumar BH, Raghuprasad BK, Ramachandramurthy DS, Narayanan R, Gopalakrishnan S. Effect of fly ash and slag on the fracture characteristics of high-performance concrete. Mater Struct. 2005; 38(1):63-72. https://doi.org/10.1007/BF02480576
34. Nikbin IM, Beygi MHA, Kazemi MT, Vaseghi Amiri J, Rahmani E, Rabbanifar S, *et al.* Effect of coarse aggregate volume on fracture behaviour of self-compacting concrete. Constr Build Mater. 2014; 52:137-45. https://doi.org/10.1016/j.conbuildmat.2013.11.041
35. Beygi MHA, Kazemi MT, Nikbin IM, Vaseghi Amiri J, Rabbanifar S, Rahmani E. The influence of coarse aggregate size and volume on the fracture behaviour and brittleness of self-compacting concrete. Cem Concr Res. 2014; 66:75-90. https://doi.org/10.1016/j.cemconres.2014.06.008
36. Prakash GB, Prashanth MH, Narasimhan MC, Mahendra K, Das AK. Flexural and fracture performance of fibre reinforced self-compacting alkali activated concrete - a DOE approach. Theor Appl Fract Mech. 2024; 133:104630. https://doi.org/10.1016/j.tafmec.2024.104630
37. El-Hassan H, Elkholy S. Enhancing the performance of alkali-activated slag-fly ash blended concrete through hybrid steel fibre reinforcement. Constr Build

Mater. 2021; 311:125313. https://doi.org/10.1016/j.conbuildmat.2021.125313
38. Nikbin IM, Beygi MHA, Kazemi MT, Vaseghi Amiri J, Rahmani E, Rabbanifar S, *et al.* A comprehensive investigation into the effect of ageing and coarse aggregate size and volume on mechanical properties of self-compacting concrete. Mater Des. 2014; 59:199-210. https://doi.org/10.1016/j.matdes.2014.02.054
39. Joseph B, Mathew G. Influence of aggregate content on the behaviour of fly ash-based geopolymer concrete. Scientia Iranica. 2012; 19(5):1188-94. https://doi.org/10.1016/j.scient.2012.07.006
40. Sabir BB. On the tortuosity of the fracture surface in concrete. Eng Fract Mech. 1997; 22(6):785-95. https://doi.org/10.1016/S0008-8846(97)00063-X
41. Gao X, Yu QL, Brouwers HJH. Reaction kinetics, gel character and strength of ambient temperature cured alkali activated slag-fly ash blends. Constr Build Mater. 2015; 80:105-15. https://doi.org/10.1016/j.conbuildmat.2015.01.065
42. Zhang H, Sarker PK, Wang Q, He B, Jiang Z. Comparative fracture properties of ambient-cured geopolymer concrete containing four different fibres in mono and hybrid combinations using digital image correlation. J Build Eng. 2024; 89:109288. https://doi.org/10.1016/j.jobe.2024.109288
43. Beygi MHA, Kazemi MT, Vaseghi Amiri J, Nikbin IM, Rabbanifar S, Rahmani E. Evaluation of the effect of maximum aggregate size on fracture behaviour of self-compacting concrete. Constr Build Mater. 2014; 55:202-11. https://doi.org/10.1016/j.conbuildmat.2014.01.065
44. Bondar D, Basheer M, Nanukuttan S. Suitability of alkali-activated slag/fly ash (AA-GGBS/FA) concretes for chloride environments: characterisation based on mix design and compliance testing. Constr Build Mater. 2019; 216:612-21. https://doi.org/10.1016/j.conbuildmat.2019.05.043
45. Xie J, Wang J, Rao R, Wang C, Fang C. Effects of combined usage of GGBS and fly ash on workability and mechanical properties of alkali activated geopolymer concrete with recycled aggregate. Compos B Eng. 2019; 164:179-90. https://doi.org/10.1016/j.compositesb.2018.11.067
46. Lam L, Wong YL, Poon CS. Effect of fly ash and silica fume on compressive and fracture behaviours of concrete. Cem Concr Res. 1998; 28(2):271-83. https://doi.org/10.1016/S0008-8846(97)00269-X
47. Molaei Raisi E, Vaseghi Amiri J, Davoodi MR. Influence of rice husk ash on the fracture characteristics and brittleness of self-compacting concrete. Eng Fract Mech. 2018; 199:595-608. https://doi.org/10.1016/j.engfracmech.2018.06.025
48. Patel YJ, Shah N. Enhancement of the properties of ground granulated blast furnace slag-based self-compacting geopolymer concrete by incorporating rice husk ash. Constr Build Mater. 2018; 171:654-62. https://doi.org/10.1016/j.conbuildmat.2018.03.166
49. Ghasemi M, Ghasemi MR, Mousavi SR. Investigating the effects of maximum aggregate size on self-compacting steel fibre reinforced concrete fracture parameters. Constr Build Mater. 2018; 162:674-82. https://doi.org/10.1016/j.conbuildmat.2017.11.141
50. Bazant ZP, Kazemi MT. Size effect in fracture of ceramics - determination of fracture energy and effective process zone length. J Am Ceram Soc. 1990; 73(7):1841-53. https://doi.org/10.1111/j.1151-2916.1990.tb05233.x